Resolving small-scale structures in Boussinesq convection by high resolution numerical methods

Wai Sun Don [*]

Brown University, Division of Applied Mathematics,
Providence, RI 02912, USA. wsdon@cfm.brown.edu

Tao Tang [†]

Department of Mathematics, Hong Kong Baptist University
Kowloon Tong, Hong Kong. ttang@math.hkbu.edu.hk.

Zhenru Zhang [‡]

Department of Mathematics, Hong Kong Baptist University
Kowloon Tong, Hong Kong. zrzhang@math.hkbu.edu.hk.

April 16, 2004

Abstract

Inviscid Boussinesq convection is a challenging problem both analytically and numerically. Due to the complex dynamic development of small scales and the rapid lose of solution regularity, Boussinesq convection pushes any numerical strategy to the limit. In E & Shu [*Phys. Fluids*, 6 (1994), pp. 49-58], a detailed numerical study of the Boussinesq convection in the absence of viscous effects is carried out using filtered pseudospectral method and a high-order accurate ENO schemes. The goal of this work is to capture a possible finite-time blow-up of the Boussinesq solutions. To this end, we will employ two high resolution methods, namely moving mesh method and Fourier collocation method with postprocessing, to compute inviscid Boussinesq problem. The moving mesh method is found useful in resolving small structures with reasonably small number of grid points. The spectral methods with Fourier-Padé reconstruction is found powerful in obtaining large time solutions, which can

remove small oscillations around the sharp fronts of the solutions. At $t = 4$, a finite-time blow-up is observed numerically. Although the possibility that the blow-up is a numerical artifact can not be ruled out, the results do agree with some recent computations using the adaptive mesh refinement techniques with extremely fine meshes.

1   Introduction

There are several reasons for the study of two-dimensional Boussinesq convection. For example, it is a simple model to address the open problem about whether finite time singularity occurs for initially smooth flows in inviscid and incompressible 3-D Euler flows. The governing equations of Boussinesq convection are analogous to those of 3D axis-symmetric Euler flow with swirl, see, e.g., [25, 26]. The understanding of finite-time singularities may be crucial to explain small scale structures in viscous turbulent flows. The Boussinesq convection has also potential relevance to the study of atmospheric and oceanography turbulence, as well as other astrophysical situations where rotation and stratification play a dominant role. As previous numerical studies have shown [9, 14, 19, 20, 21], the complex dynamics and the rapid formation of small scales make this problem an extremely demanding test for any numerical techniques.

The question of whether there exists a finite-time blow-up of the vorticity and temperature gradient has been numerically investigated by several authors. Pumir and Sigga [25] predicted a finite-time blow-up using an adaptive mesh refinement (AMR) method. However, the ENO and spectral computations of E & Shu [14] and the moving mesh computations of Ceniceros & Hou [9] did not observe the blow-up phenomena. On the other hand, a recent computation performed by Yamada et al. [32] uses $2^{21} \approx 10^6$ effective grid-points in each direction, which suggests that the temperature gradient and vorticity blows up at rates $(t_0 - t)^{-2}$ and $(t_0 - t)^{-1}$, respectively. The numerical method used in [32] is the adaptive mesh refinement technique of Berger & Oliger [4].

The goal of this work is to capture some possible finite-time blow-up of the Boussinesq problem with some careful numerical studies. To this end, we will employ two high resolution numerical methods, namely the moving mesh method and the Fourier spectral method. The moving mesh methods keep the total number of the grid points fixed. The mesh grids are moved continuously in the whole solution domain to cluster grid points in regions where the solution has the largest variations. In the past two decades this numerical technique has been proven very powerful for solving time-dependent problems whose solution has large gradients or discontinuities, see, e.g., [1, 8, 9, 22]. In this work, a moving mesh method developed in [33] will be employed. The adaptive mesh is obtained by solving a set of nonlinear elliptic PDEs for the mesh map, and a conservative interpolation is used to obtain the approximate solution on the resulting adaptive mesh. The given PDEs are advanced in time using a second-order finite-volume approach. The main purpose is to

develop a simple yet efficient adaptive strategy for solving the incompressible flow that may develop solution singularities.

The second numerical method used in this work is an adaptation of the standard Fourier pseudospectral (collocation) method for compressible flow (see, e.g., [11]) to the incompressible inviscid Boussinesq problem with possible existence of singularity. The Fourier methods are powerful for approximating periodic analytic functions with spectral convergence. However, for periodic piecewise analytic functions the well known difficulty of the Fourier methods is the oscillations near singularity called Gibbs phenomenon [17, 18]. It has been shown that the Gibbs effect can be essentially removed by using a Fourier-Padé reconstruction, see, e.g., [16, 24]. This work will further develop the Fourier-Padé postprocessing procedure to remove small oscillations around the sharp fronts in the solutions.

This paper is organized as follows. In Section 2, the system of the incompressible Boussinesq equations will be given, together with the initial and boundary conditions. In Section 3, a moving mesh strategy will be described, which will be applied to simulate the Boussinesq convection problem. In Section 4, we briefly present the Fourier collocation methods for discontinuous solutions together with the Fourier-Padè reconstruction technique. In Section 5, numerical results obtained by using the methods described in Sections 3 and 4 will be presented and discussed. Concluding remarks will be given in the final section.

2 The Boussinesq problem

The two-dimensional Boussinesq convection in the absence of viscous effects have the form

$$\text{(2.1)} \qquad \rho_t + \mathbf{u} \cdot \nabla \rho = 0,$$

$$\text{(2.2)} \qquad \mathbf{u}_t + \mathbf{u} \cdot \nabla \mathbf{u} = -\nabla p + \rho g \mathbf{j},$$

$$\text{(2.3)} \qquad \nabla \cdot \mathbf{u} = 0,$$

where p is the pressure, ρ is the density (usually this should be the temperature and denoted by T or θ, but we are accustomed to call it density, and therefore denote it by ρ), $\mathbf{u} = (u, v)$ is the velocity, g is the gravitational constant, and $\mathbf{j}$ is the unit vector in the upward vertical direction. In 2-D, the above system of equations can be re-written using the stream function-vorticity formulation. Let $\omega = v_x - u_y$ be the vorticity, the velocity $\mathbf{u} = (u, v)$ is determined by the stream function ψ:

$$\text{(2.4)} \qquad u = \psi_y, \qquad v = -\psi_x.$$

By normalizing the gravitational constant g to be 1, the Boussinesq system (2.1)-(2.3) can be written as

$$\text{(2.5)} \qquad \rho_t + \mathbf{u} \cdot \nabla \rho = 0,$$

3

$$(2.6) \qquad \qquad \omega_t + \mathbf{u} \cdot \nabla \omega = -\rho_x \, ,$$

$$(2.7) \qquad \qquad -\Delta \psi = \omega.$$

The above system can also be written in the conservative form which is more suitable for the Fourier Pseudospectral (collocation) methods. In the absence of numerical dissipation, the conservative form will guarantee the conservation of the conservative quantities even in the presence of singularity [5, 6]. In the conservative form, the system (2.5)-(2.7) becomes

$$(2.8) \qquad \qquad \rho_t + \nabla \cdot (\rho \mathbf{u}) = 0,$$

$$(2.9) \qquad \qquad (\rho \omega)_t + \nabla \cdot (\rho \omega \mathbf{u}) = -\frac{1}{2} \left(\rho^2 \right)_x \, ,$$

$$(2.10) \qquad \qquad -\Delta \psi = \omega.$$

Several existing studies show that this problem is extremely difficult both numerically and analytically. Although short time existence can be shown for sufficiently smooth initial conditions, it is unclear whether a solution will lose regularity and become singular in a finite time. Following Beale et al. [3], E & Shu [14] proved that if a singularity develops in the Boussinesq flow at a finite time T^* satisfying $\|\mathbf{u}(\cdot, T^*)\|_m + \|\rho(\cdot, T^*)\|_m = +\infty$ then

$$(2.11) \qquad \int_0^{T^*} |\omega(\cdot, t)|_\infty dt = +\infty \qquad \int_0^{T^*} \int_0^t |\rho_x(\cdot, s)|_\infty ds dt = +\infty$$

where $\|f(\cdot)\|_m$ is the standard m-norm in the Sobolev space and $|\cdot|_\infty$ is the maximum-norm in $\mathbf{R}^2$. E & Shu also made a very comprehensive numerical study on small-scale structures using two high resolution numerical methods, namely a filtered Fourier pseudospectral method and a third-order ENO scheme. Their numerical results show that the sharp fronts are developed in a later time from a smooth initial profile although a finite-time blow-up is not seen in their computations.

In this work, we will use the same initial conditions as that in [14]:

$$(2.12) \qquad \omega(x, y, 0) = 0, \qquad \rho(x, y, 0) = 50 \rho_1(x, y) \rho_2(x, y)[1 - \rho_1(x, y)],$$

where

$$\rho_1(x, y) = \begin{cases} \exp \left(1 - \dfrac{\pi^2}{\pi^2 - x^2 - (y - \pi)^2} \right) & x^2 + (y - \pi)^2 \leq \pi^2 \\ 0 & \text{otherwise} \end{cases}$$

$$\rho_2(x, y) = \begin{cases} \exp \left(1 - \dfrac{(1.95\pi)^2}{(1.95\pi)^2 - (x - 2\pi)^2} \right) & |x - 2\pi| < 1.95\pi, \\ 0 & \text{otherwise} \end{cases}$$

The initial density contour is plotted in Fig. 1. A double 2π periodic boundary condition on both sides of the square domain is assumed. For the smooth initial data (2.12), the numerical solution of the Boussinesq system remains smooth until $t \approx 2.0$. As the bubble rises, the front of the bubble steepen up into a sharp gradient. Large amount of vorticity are generated and deposited around the sharp density edge due to the production of vorticity in the source terms of the vorticity equation.
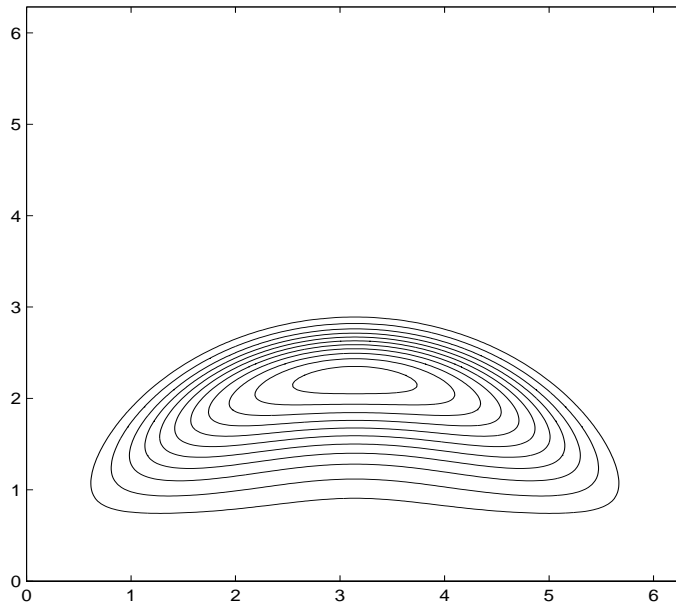
4

Figure 1: Initial density contours.

3   Moving mesh method

In Zhang & Tang [34], an efficient moving mesh algorithm is developed for solving convection-diffusion problems with small viscosity, which will be used to solve the 2D Boussinesq problems. In principle, our adaptive grid algorithm is formed by two independent parts: a mesh re-distribution part and a PDE evolution part, which is demonstrated in Table I. The idea of the present approach is to solve both the mesh equation and the underlying PDEs on the computational (i.e. logical) domain. This approach enables us to solve the Poisson equation (2.7) with some faster solvers such as multigrid methods.

3.1   Mesh redistribution

The solution-adaptive mesh is obtained through a bijective map from a logical or computational domain to the physical domain. A fixed uniform mesh is used in the logical domain. Denote by $x(\xi, \eta)$ and $y(\xi, \eta)$ the mesh map in two dimensions, where (ξ, η) are the coordinates in the logical domain. In the variational approach, the adaptive mesh is to find the minimizer of the following functional:

$$E[\xi, \eta] = \frac{1}{2} \int_{\Omega_p} [\nabla \xi^T G_1^{-1} \nabla \xi + \nabla \eta^T G_2^{-1} \nabla \eta] dx dy$$

where G_1 and G_2 are given symmetric positive definite matrices, and Ω_p is the solution domain in the physical space. More terms can be added to the variational form to control the property of the adaptive mesh [7]. Minimizing the above functional leads to the

5

Table I: Outline of the numerical algorithm

---

0. Determine the initial mesh based on the initial function.

1. Determine Δt based on CFL-type condition so that $t^{n+1} = t^n + \Delta t$.

2. Advance the solution one time step based on an appropriate numerical scheme.

3. Grid Restructuring

    a. Solve the mesh redistributing equation (a generalized Laplace equation) by one Gauss-Seidel iteration, to get $\mathbf{x}^{(k),n}$

    b. Interpolating the approximate solutions on the new grid $\mathbf{x}^{(k),n}$

    c. A weighted average of the locally calculated monitor at each computational cell and the surrounding monitor values

    d. The above iteration procedure (a.)-(c.) on grid-motion and solution-interpolation is continued until there is no significant change in calculated new grids from one iteration to the next.

Start new time step (go to **1** above).

---

following Euler-Lagrange equations:

$$(3.1) \qquad \nabla \cdot (G_1^{-1} \nabla \xi) = 0, \qquad \nabla \cdot (G_2^{-1} \nabla \eta) = 0.$$

One of the simplest choices of the monitor functions is of scalar type: $G_1 = G_2 = \Omega I$, where I is the identity matrix and $\Omega > 0$ is called a monitor function. One typical choice of the monitor function is $\Omega = \sqrt{1 + |\nabla u|^2}$, where u is a solution of the underlying PDEs. This choice of the monitor function corresponds to Winslow's variable diffusion method [31]. The mesh generation equation (3.1) is defined in the physical domain Ω_p. In practice, Ω_p may be very complex and as a result it is difficult to solve the elliptic system (3.1) directly. To overcome this difficulty, we follow Ceniceros & Hou [9] to consider a functional defined in the computational domain:

$$(3.2) \qquad \tilde{E}[x, y] = \frac{1}{2} \int_{\Omega_c} (\tilde{\nabla} x^T G_1 \tilde{\nabla} x + \tilde{\nabla} y^T G_2 \tilde{\nabla} y) d\xi d\eta,$$

where $\tilde{\nabla} = (\partial_\xi, \partial_\eta)^T$. The corresponding Euler-Lagrange equations are of the form

$$(3.3) \qquad (G_1 x_\xi)_\xi + (G_1 x_\eta)_\eta = 0, \quad (G_2 y_\xi)_\xi + (G_2 y_\eta)_\eta = 0.$$

If we choose $G_1 = G_2 = \Omega I$, then the equation (3.3) is reduced to:

$$(3.4) \qquad \tilde{\nabla} \cdot (\Omega \tilde{\nabla} x) = 0, \qquad \tilde{\nabla} \cdot (\Omega \tilde{\nabla} y) = 0.$$

6

In practical computations, it suffices to obtain some approximate solutions for the above equations at each time step. One possibility is to perform a few (about 3) Gauss-Seidel (GS) iterations at each time level. The iteration is continued until there is no significant change in calculating new grids from one iteration to the next. After each GS iteration step, we need to pass the solution information from the old mesh $(x_{j,k}, y_{j,k})$ to the newly obtained mesh $(\tilde{x}_{j,k}, \tilde{y}_{j,k})$. This is done by using the conservative interpolation proposed by Tang & Tang [29]:

$$(3.5) \qquad |\tilde{A}_{j+\frac{1}{2},k+\frac{1}{2}}|\tilde{u}_{j+\frac{1}{2},k+\frac{1}{2}} = |A_{j+\frac{1}{2},k+\frac{1}{2}}|u_{j+\frac{1}{2},k+\frac{1}{2}}$$
$$- \left[(c^x u)_{j+1,k+\frac{1}{2}} - (c^x u)_{j,k+\frac{1}{2}}\right] - \left[(c^y u)_{j+\frac{1}{2},k+1} - (c^y u)_{j+\frac{1}{2},k}\right]$$

where $c^x_{j,k} = x_{j,k} - \tilde{x}_{j,k}, c^y_{j,k} = y_{j,k} - \tilde{y}_{j,k}$, $|A|$ denotes the volume size of A. The derivation of the formula (3.5) and some of its theoretical properties can be found in [29]. It is obvious that (3.5) satisfies the mass-conservation property in the following sense:

$$\sum_{j,k} |\tilde{A}_{j+\frac{1}{2},k+\frac{1}{2}}|\tilde{u}_{j+\frac{1}{2},k+\frac{1}{2}} = \sum_{j,k} |A_{j+\frac{1}{2},k+\frac{1}{2}}|u_{j+\frac{1}{2},k+\frac{1}{2}}.$$

3.2 Numerical solution to PDEs

The governing equations of the Boussinesq equations are of conservative form. To demonstrate the principal ideas for the PDE evolution, let us consider the 2-D conservation system:

$$(3.6) \qquad u_t + f(u)_x + g(u)_y = 0 \qquad (x,y) \in \Omega_p \,.$$

To allow flexibility of handling complex geometry and of using fast solution solvers, we first transform the underlying PDEs using the coordinate transformations $x = x(\xi, \eta), y = y(\xi, \eta)$ and then solve the resulting equations in the computational domain equipped with a (fixed) uniform mesh. The cell-centered finite volume method will be employed to solve the transformed PDEs. Note that

$$u_x = \frac{1}{J}\left[(y_\eta u)_\xi - (y_\xi u)_\eta\right], \qquad u_y = \frac{1}{J}\left[-(x_\eta u)_\xi + (x_\xi u)_\eta\right],$$

where $J = x_\xi y_\eta - x_\eta y_\xi$ is the Jacobian of the coordinate transformation. With the above formulas, the underlying equation (3.6) becomes:

$$(3.7) \qquad u_t + \frac{1}{J}\left(y_\eta f(u) - x_\eta g(u)\right)_\xi + \frac{1}{J}\left(x_\xi g(u) - y_\xi f(u)\right)_\eta = 0 \qquad (\xi, \eta) \in \Omega_c$$

where Ω_c is the computational domain with a uniform grid (ξ_j, η_k). For convenience, we write the above equation in a compact form:

$$(3.8) \qquad u_t + \frac{1}{J}F(u)_\xi + \frac{1}{J}G(u)_\eta = 0.$$

The above system will be solved by using a finite-volume approach. Denote the control cell $[\xi_j\,,\xi_{j+1}] \times [\eta_k\,,\eta_{k+1}]$ by $A_{j+\frac{1}{2},k+\frac{1}{2}}$ and the cell average value by

$$\bar{u}^n_{j+\frac{1}{2},k+\frac{1}{2}} = \frac{1}{\Delta\xi\Delta\eta} \int_{A_{j+\frac{1}{2},k+\frac{1}{2}}} u(\xi,\eta,t^n)d\xi d\eta\,.$$

Note that

$$\frac{1}{\Delta\xi\Delta\eta} \int_{\xi_j}^{\xi_{j+1}} \int_{\eta_k}^{\eta_{k+1}} \frac{1}{J} w_\xi d\xi d\eta$$

$$= \frac{1}{\Delta\xi\Delta\eta} \frac{1}{J_{j+\frac{1}{2},k+\frac{1}{2}}} \int_{\xi_j}^{\xi_{j+1}} \int_{\eta_k}^{\eta_{k+1}} w_\xi d\xi d\eta + \mathcal{O}(\Delta\xi^2)$$

$$= \frac{1}{J_{j+\frac{1}{2},k+\frac{1}{2}}} \left(\frac{w_{j+1,k+\frac{1}{2}} - w_{j,k+\frac{1}{2}}}{\Delta\xi} \right) + \mathcal{O}(\Delta\xi^2)$$

where a mid-point rule is used in the first step. Similar approach can be used to treat the term involving $J^{-1}w_\eta$. Integrating equation (3.8) over the cell $[t^n, t^{n+1}] \times A_{j+\frac{1}{2},k+\frac{1}{2}}$ in the computational domain yields

$$(3.9) \quad \bar{u}^{n+1}_{j+\frac{1}{2},k+\frac{1}{2}} = \bar{u}^n_{j+\frac{1}{2},k+\frac{1}{2}} - \frac{\Delta t^n}{J_{j+\frac{1}{2},k+\frac{1}{2}}} \left(\frac{\bar{F}^n_{j+1,k+\frac{1}{2}} - \bar{F}^n_{j,k+\frac{1}{2}}}{\Delta\xi} + \frac{\bar{G}^n_{j+\frac{1}{2},k+1} - \bar{G}^n_{j+\frac{1}{2},k}}{\Delta\eta} \right).$$

The one-dimensional Lax-Friedrich numerical flux

$$\bar{f}(a,b) = \frac{1}{2}[f(a) + f(b) - \max|f'(u)|(b-a)],$$

where the maximum is taken between a and b, will be applied to $\bar{F}$, $\bar{G}$ respectively:

$$(3.10) \qquad \bar{F}_{j,k+\frac{1}{2}} = \bar{F}(u^-_{j,k+\frac{1}{2}}, u^+_{j,k+\frac{1}{2}}), \qquad \bar{G}_{j,k+\frac{1}{2}} = \bar{G}(u^-_{j,k+\frac{1}{2}}, u^+_{j,k+\frac{1}{2}}).$$

To compute (3.10), a piecewise linear approximation will be used:

$$u^-_{j,k+\frac{1}{2}} = \bar{u}_{j-\frac{1}{2},k+\frac{1}{2}} + \frac{\Delta\xi}{2} s_{j-\frac{1}{2},k+\frac{1}{2}}, \qquad u^+_{j,k+\frac{1}{2}} = \bar{u}_{j+\frac{1}{2},k+\frac{1}{2}} - \frac{\Delta\xi}{2} s_{j+\frac{1}{2},k+\frac{1}{2}}$$

$$s_{j+\frac{1}{2},k+\frac{1}{2}} = \left(\text{sign}(s^-_{j+\frac{1}{2},k+\frac{1}{2}}) + \text{sign}(s^+_{j+\frac{1}{2},k+\frac{1}{2}}) \right) \frac{|s^+_{j+\frac{1}{2},k+\frac{1}{2}} s^-_{j+\frac{1}{2},k+\frac{1}{2}}|}{|s^+_{j+\frac{1}{2},k+\frac{1}{2}}| + |s^-_{j+\frac{1}{2},k+\frac{1}{2}}|}$$

$$s^-_{j+\frac{1}{2},k+\frac{1}{2}} = \frac{\bar{u}_{j+\frac{1}{2},k+\frac{1}{2}} - \bar{u}_{j-\frac{1}{2},k+\frac{1}{2}}}{\Delta\xi} \qquad s^+_{j+\frac{1}{2},k+\frac{1}{2}} = \frac{\bar{u}_{j+\frac{3}{2},k+\frac{1}{2}} - \bar{u}_{j+\frac{1}{2},k+\frac{1}{2}}}{\Delta\xi}\,.$$

A system of semi-discretized equations can be obtained from the fully discretized scheme (3.9), which will be solved by an 3-stage Runge-Kutta method proposed by Shu & Osher [28]. This ODE solver satisfies the total variation non-increasing property.

4 Fourier collocation methods with postprocessing

As an independent check, we will also solve the Boussinesq problem by using the Fourier collocation methods. This approach is particularly suitable since the physical setup of the proposed problem is periodic in both directions. The proposed spectral algorithm is stabilized by using a high order exponential filter. An essentially non-oscillatory solution at the desirable time step and locations can be reconstructed by the newly developed Fourier-Padé postprocessing procedure proposed by Min et al. [24].

4.1 The Fourier collocation methods

For the Boussinesq equations, the dependent variables ρ, ω, u, v and ψ are discretized uniformly in space at the Fourier-Gauss-Lobatto collocation points,

$$(4.1) \qquad x_i = \frac{\pi i}{N}, \quad y_j = \frac{\pi j}{N}, \quad i,j = 0,\ldots,2N-1$$

and for simplicity we will use the same number of collocation points in both x and y directions. Furthermore, we assume that the variables can be expressed in the tensor product form. Hence, the evaluation of the variables and the fluxes can be treated along each dimension separately and independently. The dependent variables, say $f(x) = \rho(x,\cdot,\cdot,$ for are interpolated at the collocation points, i.e.,

$$(4.2) \qquad f_N(x) = \sum_{j=0}^{2N-1} f(x_j) g_j(x)$$

where $g_j(x)$ is the trigonometric interpolation polynomial of degree N,

$$(4.3) \qquad g_j(x) = \frac{1}{2N} \sin N(x - x_j) \cot \frac{(x - x_j)}{2}.$$

It can be verified that $g_j(x_k) = \delta_{j,k}$. It follows from (4.2) that

$$(4.4) \qquad \frac{d}{dx} f_N(x_k) = \sum_{j=0}^{2N-1} f(x_j) g_j'(x_k), \qquad 0 \leq k \leq 2N - 1.$$

The elements of the resulting $2N \times 2N$ differentiation matrix $\mathbf{D}$, $\mathbf{D}_{jk} = g_j'(x_k)$, are given by

$$(4.5) \qquad \mathbf{D}_{jk} = \begin{cases} 0 & k = j, \\ \frac{1}{2}(-1)^{j+k} \cot \frac{(x_k - x_j)}{2} & k \leq j. \end{cases}$$

Since the physical flow is (anti-)symmetric along the mid-plane $(x = \pi)$ in the x-direction, we have $\rho(\pi + x, y, t) = \rho(\pi - x, y, t), \omega(\pi + x, y, t) = -\omega(\pi - x, y, t)$. It follows that the computation time can be halved in the spectral algorithm. The data length along the

9

x-direction will be halved ($0 \leq i \leq N$) and the $2N \times 2N$ differentiation matrix $\mathbf{D}$ can be decomposed into even one $\mathbf{D}_E$ and odd one $\mathbf{D}_O$ with size $(N+1) \times (N+1)$ each. The odd and even sub-matrices will be operated on anti-symmetric and symmetric data structures, respectively. An efficient and accurate formula for computing the first and higher order differentiation matrices can be found in [10, 17].

In above we have presented differentiation matrix formulation for computing the derivative of a periodical (anti-)symmetric function. It should be noted that in this case the Fast Sine (Cosine) Transforms can also be employed to accomplish the same task and will result in a more efficient algorithm for large number of collocation points, say $N > 64$. For an even (odd) function, the real (imaginary) part of the Fourier coefficients are computed first by the Fast Cosine (Sine) Transform, then multiplied by $-k$ (k) and finally transformed back to the physical space by the Fast Sine (Cosine) Transform.

4.2 Filter

As we have mentioned earlier, the initially smooth flow will eventually develop into a sharp front in a later time. This leads to two major consequences for the spectral approaches. The first one is the appearance of small persistence oscillations around the sharp front, which is known as the Gibbs phenomenon. The second one is related to the stability of the numerical scheme. The energy contained in the high frequencies regime will grow quickly and the scheme will eventually becomes unstable. The reason is that the Fourier methods are conservative and do not possess any numerical dissipation. All resolvable modes are captured exactly in the absence of aliasing error. It is a great advantage when the flow is well-resolved by the spectral methods. For highly non-linear problems, it could become a great disadvantage as the non-linear interaction of modes generates modes that spread over the whole solution spectrum. This leads to the well known non-linear instability as the high frequencies (usually associated with noise and error) grow unbounded in time. To address the second problem, a small amount of filtering will be applied to remove the excess growth of the high frequencies as proposed by Vandeven [30]. Given the Fourier approximation

$$f_N(x) = \sum_{k=-N}^{N} \hat{f}_k e^{i\pi k x},$$

we construct a filtered sum

$$(4.6) \qquad f_N^{\sigma}(x) = \sum_{k=-N}^{N} \sigma(k) \hat{f}_k e^{i\pi k x}$$

where $\sigma(k)$ is a low pass filter. The favorite one we preferred to use is the exponential filter which is of the form

$$(4.7) \qquad \sigma(k) = \exp\left(-\alpha \left| k/N \right|^{\beta}\right)$$

where $|k| = 0, \ldots, N$, $\alpha = -\ln \epsilon$, ϵ is the machine zero and β is the order of the filter. We used $\beta = 16$ in this study. The exponential filter offers the flexibility of changing the order of the filter by simply specifying a different value of β [30].

In addition to apply filtering on the dependent variables, filtering is also applied to the fluxes to enhance the stability of the spectral scheme. Though an explicit formula cannot be written down for the addition of the filter into the differentiation matrix, the filtered differentiation matrix can be directly computed in a fairly straightforward manner by performing the differentiation on the direct sum of (4.6) and making use of the fact that the filter $\sigma(k)$ is symmetric about $k = 0$.

4.3   Time Marching and Poisson Solver

For time marching, we use the low storage third order TVD Runge-Kutta scheme of Shu & Osher [28], which is stable for $\Delta t \approx \mathcal{O}(N^{-1})$. The time step $\Delta t = 0.001$ is used in the simulations. At the end of each Runge-Kutta stage, the Poisson equation (2.7) is solved to update the new velocity field (u, v). After the discretization with the Fourier collocation methods, the Poisson equation (2.7) in the physical space can be expressed in a matrix equation form

$$(4.8) \qquad\qquad\qquad \mathbf{A}\psi + \psi\mathbf{B} = -\omega$$

where the matrices $\mathbf{A}$ and $\mathbf{B}^T$ are the second order Fourier differentiation matrix in the x and y directions respectively. Given a vorticity field $\omega(x_i, y_j)$, the matrix equation solver ABSLV is used to solve the above linear system. The matrices $\mathbf{A}$ and $\mathbf{B}$ are casted in the lower and upper Schur form and the transformed system is solved by backward substitution as described in [2]. This may not be the most efficient way to solve the Poisson equations with periodic boundary conditions, but it is also applicable to problems with non-periodic solutions. The original code ABSLV can be obtained from the software depository at NETLIB. The code is slightly modified to enhance the precision and the error tolerance in our computations.

To facilitate an efficient and accurate computation of the Boussinesq equations with the Fourier collocation methods, we employed the PseudoPack Library developed by Costa and Don [10]. All necessary optimized routines for computing the derivatives of the flux, smoothing the dependent variables, Runge-Kutta time marching, second order differentiation matrices and the matrix equation solver are provided in the library. The detail information of the package can be found in

http://www.cfm.brown.edu/people/wsdon/home.html

4.4   Fourier-Padé postprocessing

It is known that the sharp front of the density is developed from a smooth initial profile in a later time. As a consequence, if the Fourier collocation method described above is
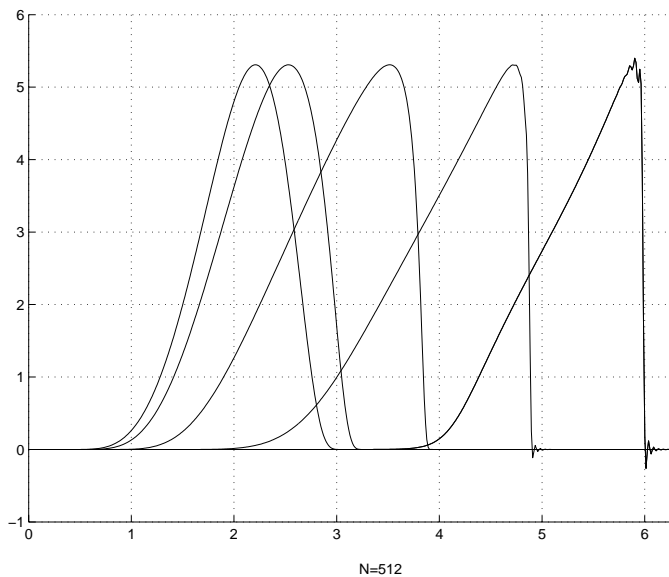
Figure 2: Evolution of density ρ along the symmetry axis $x = \pi$ by the filtered Fourier collocation method on a 512^2 grid. No postprocessing is made.

applied directly then the non-physical Gibbs oscillations will be developed. This is indeed observed in Fig. 2 where the one-dimensional cut of the density ρ at the symmetry axis $x = \pi$ from $0 \leq t \leq 3$ is shown. It is observed that the initially smooth density profile (the left most curve) is increasingly steepen up into a high gradient and eventually becomes under-resolved (the right most curve) when evolved using the Fourier collocation methods. Due to the overshoot and undershoot of the Gibbs phenomenon, the minimum ($=0$) and the maximum(≈ 5.3084) values of the density are poorly represented, see also Fig. 4.

It is now necessary to remove the Gibbs oscillations using some appropriate postprocessing procedures. It is known that the Fourier-Padé approximant offers an alternative choice of basis functions in which a periodical function can be expanded into, see , e.g., [16]. In [12], Driscoll & Fornberg recovers spectral convergence up to the discontinuity with a Fourier-Padé approach by subtracting the jumps from the Fourier data, which however requires the priori knowledge of the singularity. Below we will describe a reconstruction technique based on a Fourier-Padé approach, which does not require a priori knowledge of the jump locations. Let $\mathcal{I}_N$ be the space of the trigonometric polynomial of degree N, defined as

$$(4.9) \qquad \mathcal{I}_N = \operatorname{span}\{e^{inx}| -N \leq n \leq N - 1\}$$

at the Fourier-Gauss-Lobatto collocation points $\{x_i\}$ given by (4.1). We define the Fourier-Padé collocation approximation of u, $R_{K,M} = P_K/Q_M$, where $P_K \in \mathcal{I}_K$ and $Q_M \in \mathcal{I}_M$ ($K + 2M = N$), such that

$$(4.10) \qquad (Q_M u - P_K, v)_N = 0 \quad \forall v \in \mathcal{I}_{K+M}.$$

12

In the above equation, the discrete inner product is defined by

$$(4.11) \qquad (u, v)_N \;=\; \frac{1}{2N} \sum_{j=0}^{2N-1} u(x_j)\overline{v(x_j)}.$$

Denote

$$(4.12) \qquad P_K = \sum_{k=-K}^{K-1} \tilde{b}_k e^{ikx} \quad \text{and} \quad Q_M = \sum_{m=-M}^{M} \tilde{c}_m e^{imx}.$$

Substituting P_K, Q_M and $v = e^{inx}$, $-(K + 2M) \leq n \leq (K + 2M) - 1$, to (4.10) gives the following system of equations:

$$(4.13) \qquad \tilde{b}_k = \sum_{m=-M}^{M} \tilde{c}_m \tilde{u}_{k-m}, \;\; -K \leq k \leq K - 1$$

$$(4.14) \qquad 0 = \sum_{m=-M}^{M} \tilde{c}_m \tilde{u}_{n-m}, \;\; -K - M \leq n < -K \quad \text{and} \quad K - 1 < n \leq K - 1 + M,$$

where the Fourier coefficients $\tilde{u}_n$ are given by

$$(4.15) \qquad \tilde{u}_n \;=\; \frac{1}{2N} \sum_{j=0}^{2N-1} u(x_j) e^{-inx_j}.$$

Equations (4.13) and (4.14) yield a linear system $\tilde{A}\tilde{\mathbf{c}} = 0$ to be solved for $\tilde{\mathbf{c}}$, where $\tilde{\mathbf{c}} = [\tilde{c}_M, ..., \tilde{c}_{-M}]^T$ and

$$(4.16) \qquad \tilde{A} = \begin{pmatrix} \tilde{u}_{-K-2M} & \cdots & \tilde{u}_{-K-M} & \cdots & \tilde{u}_{-K} \\ \tilde{u}_{-K-2M+1} & \cdots & \tilde{u}_{-K-M+1} & \cdots & \tilde{u}_{-K+1} \\ \vdots & & & & \vdots \\ \tilde{u}_{-N-M-1} & \cdots & \tilde{u}_{-K-1} & \cdots & \tilde{u}_{-K+M-1} \\ \tilde{u}_{K-M+1} & \cdots & \tilde{u}_{K+1} & \cdots & \tilde{u}_{K+M+1} \\ \vdots & & & & \vdots \\ \tilde{u}_{K-1} & \cdots & \tilde{u}_{K+M-1} & \cdots & \tilde{u}_{K+2M-1} \end{pmatrix}.$$

This linear system can be solved numerically using MATLAB subroutine $\mathtt{Null}(\tilde{A})$ which gives the basis for the kernel of the $2M \times (2M + 1)$ matrix $\tilde{A}$. Once a set of the coefficients $\{\tilde{c}_m\}_{m=-M}^{M}$ is obtained, the coefficients $\{\tilde{b}_k\}_{k=-K}^{K-1}$ can be computed from Eq. (4.13). The discrete Fourier coefficients involved in computing $\tilde{b}_k$ are $\{\tilde{u}_n, \; -N + M \leq n \leq N - M - 1\}$.

In the Fourier-Padé reconstruction procedure, the Fourier modes from the top spectrum are discarded due to the fact that the lower spectrum of the Fourier modes are accurately resolved and the numerical errors are usually associated with the high modes. Thus frequencies in the upper most spectrum must be removed in order to obtain satisfactory reconstruction. To this end, we will introduce a new parameter N_c which determines the
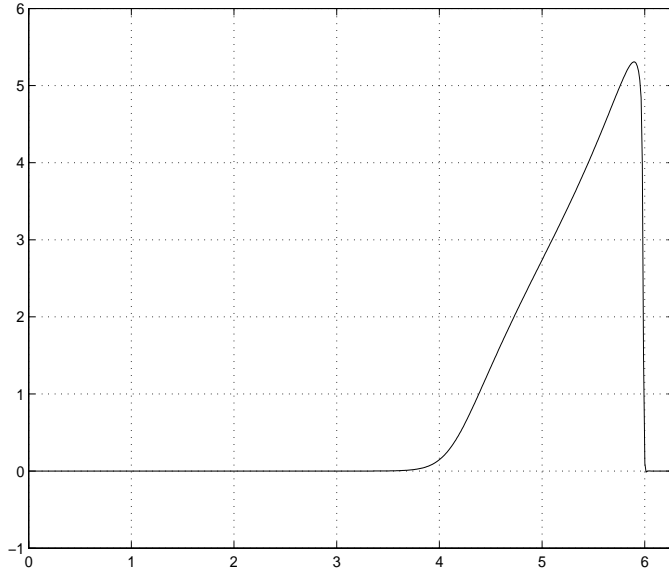
Figure 3: One dimensional cut of the density ρ along the symmetry axis $y = \pi$ at $t = 3$ using the Fourier-Padé reconstruction on a 512^2 grids.

number of low Fourier modes to be used in the reconstruction procedure. Based on the order of the exponential filter ($\beta = 16$) used in the numerical simulations, N_c is chosen to be slightly smaller than $N/3$ where N is the total number of the Fourier modes.

In Fig. 3, the Fourier-Padé reconstruction is applied to the density ρ along the symmetry axis $x = \pi$ at time $t = 3$. The reconstruction parameters are chosen as $(N_c, M) = (137, 46)$. The small oscillations around the sharp front is effectively removed, which is also demonstrated in Fig. 4 where the time history for the maximum values of the density ρ in plotted. The reconstruction parameters (N_c, M) used in the reconstruction procedure are $(64,14)$ for the 256^2-grid, $(72,24)$ for the 512^2-grid, and $(148,34)$ for the 1024^2-grid. One can observe that, for all practical purposes, the Gibbs overshoot and undershoot are effectively removed.

Fig. 5 shows the one dimensional cut of the density ρ along the symmetry axis $x = \pi$ at $t = 3$ obtained by using the Fourier collocation method with the Fourier-Padé reconstruction. The parameters used for the reconstruction are $(N_c, M) = (148, 49)$. At this time, the flow becomes very complicated with many small structures. It is clearly seen that the numerical results using Fourier-Padé reconstruction are satisfactory. It must be emphasized that the locations of the singularities do not need to be known in our Fourier-Padé reconstruction procedure as opposed to some other reconstruction algorithms.
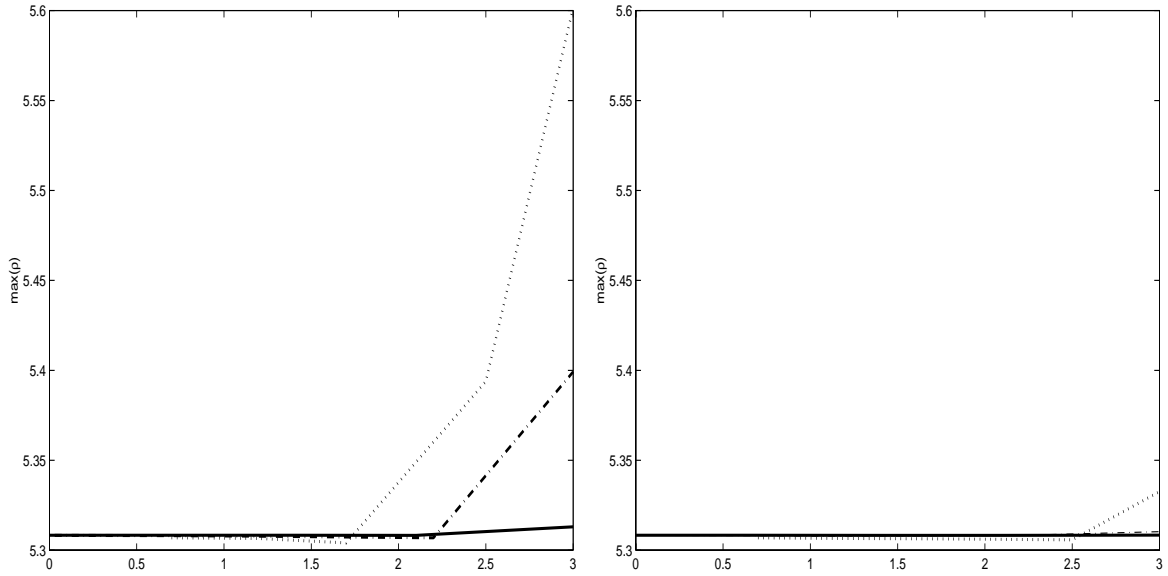
Figure 4: Time history of the maximum density ρ along the symmetry axis $x = \pi$ with the filtered Fourier collocation methods (left) and after the Fourier-Padé reconstructions (right) with a 256^2 grid (dot line), a 512^2 grid (dash-dot line), and a 1024^2 grid (solid line).
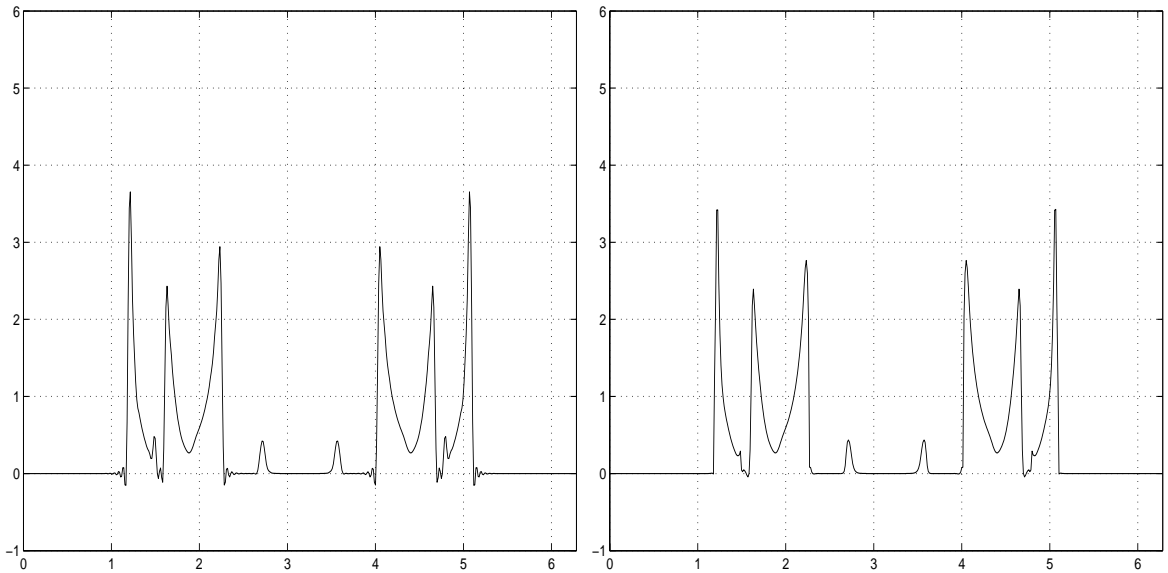

Figure 5: One dimensional cut of the density ρ at $x = \pi$ at $t = 3.0$ using filtered Fourier collocation method (left) and after the Fourier-Padé reconstruction (right), on a 512^2 grid.
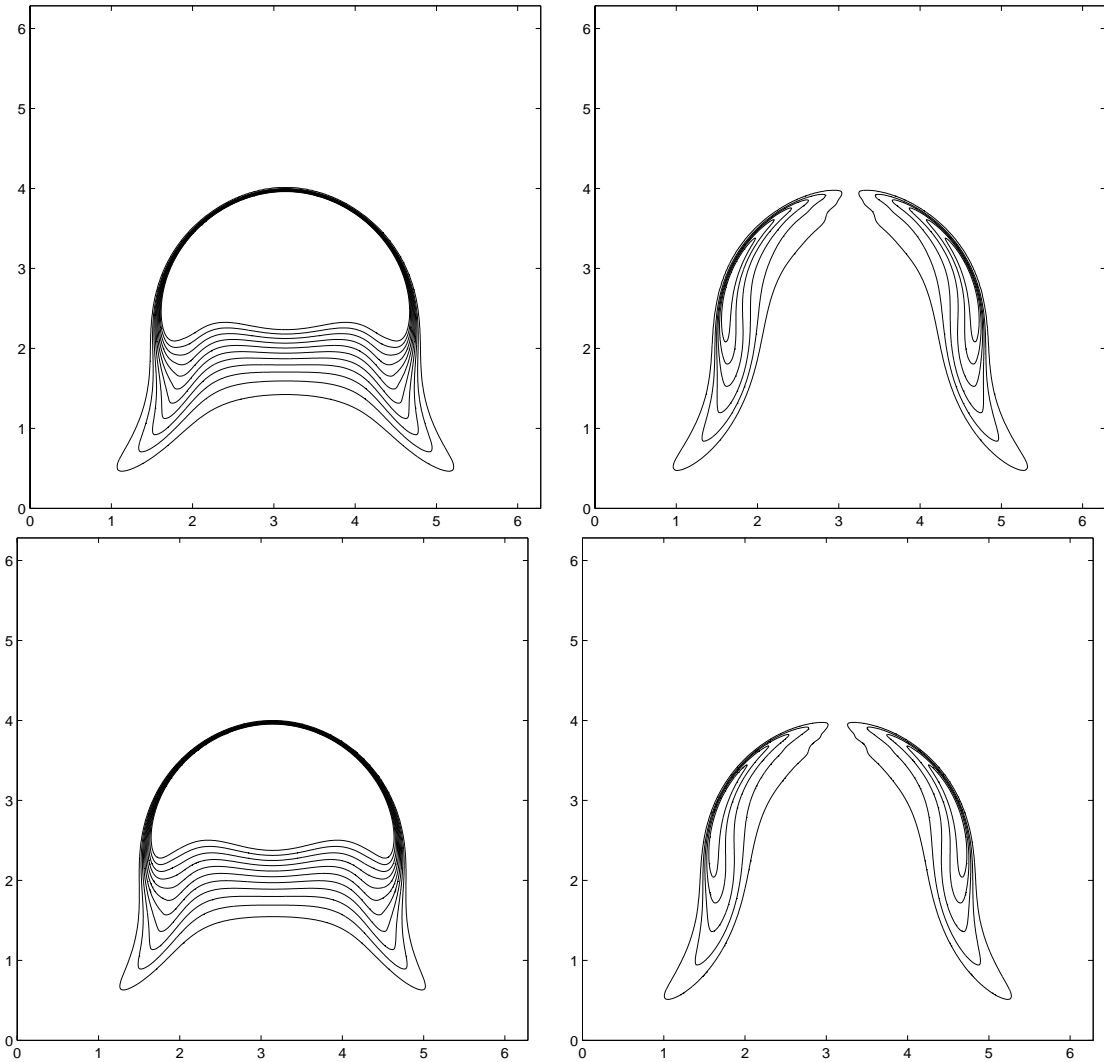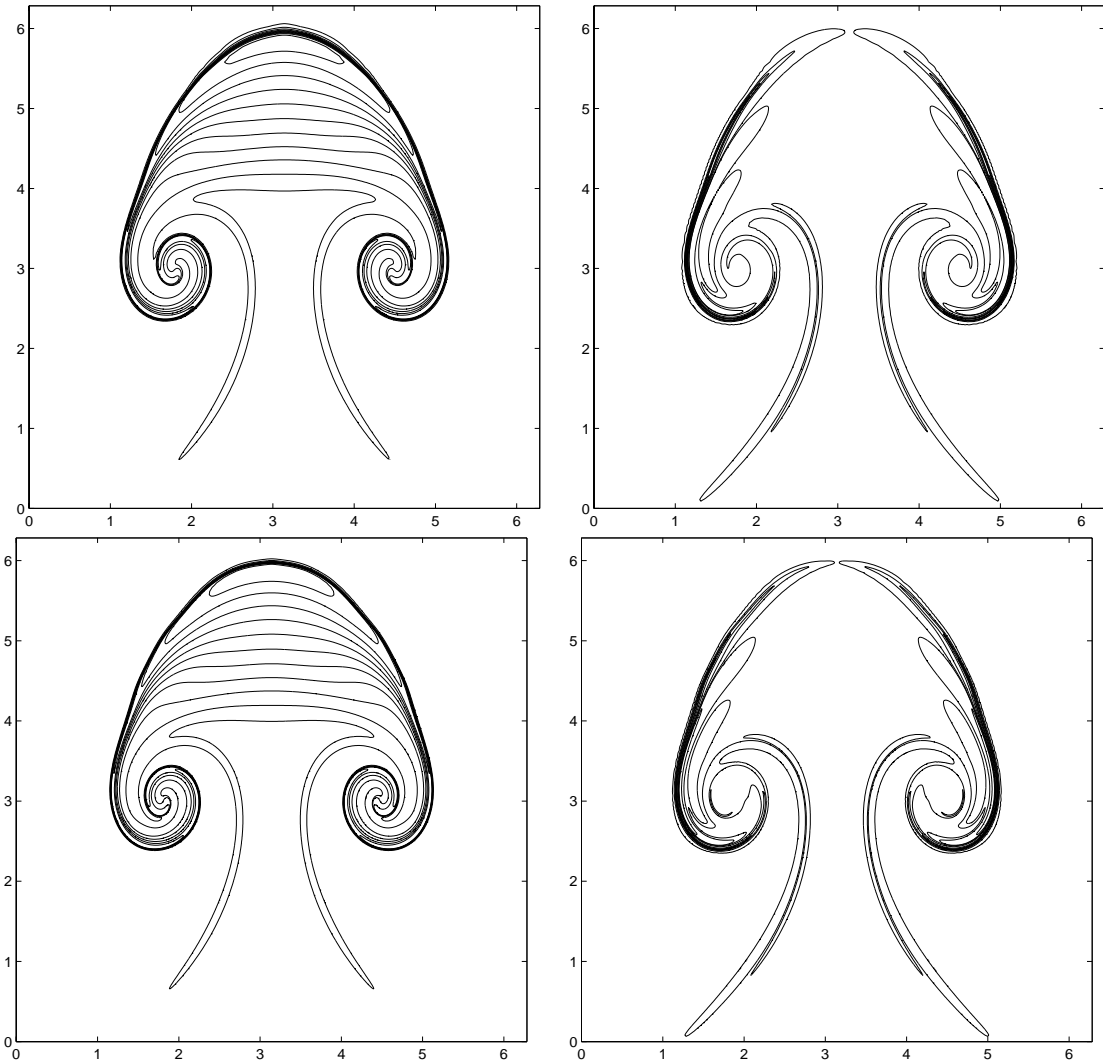
Figure 6: Moving mesh solutions at $t = 1.6$. Left: density contour; Right: vorticity contour. Top: $N_x = N_y = 300$; Bottom: $N_x = N_y = 400$.

5 Numerical Results

We will first present some moving mesh results. The monitor function used for (3.4) is $\Omega = \sqrt{1 + 0.2|\nabla\rho|^2}$. Fig. 6 shows the density and vorticity contours at $t = 1.6$ using 300^2 and 400^2 mesh points. At this time, the flow looks like a rising bubble. Graphically, there is almost no difference between the numerical solutions obtained using 300^2 and 400^2 grids, indicating that it is sufficient to resolve the flow with the 300^2 grid at this time level. The solution contours at $t = 3$ is plotted in Fig. 7. By now the outer boundary of the bubble becomes a sharp front and many small scale structures are formed. It is observed by E & Shu [14] that as the bubble rises it leaves behind a long and thin filament of light fluid. They claimed that the thin filament is a check on the amount of numerical diffusion presented in a numerical scheme: a low-order method with large numerical viscosity makes

Figure 7: Moving mesh solutions at $t = 3$. Left: density contour; Right: vorticity contour. Top: $N_x = N_y = 300$; Bottom: $N_x = N_y = 400$.

the thin filament disappeared. With our moving mesh methods the thin filament is clearly observed with 300^2 and 400^2 grids. In fact, the numerical results with the finer grids are graphically indistinguishable with those presented in [14] which were computed on a 1500^2 grid.

To see the result of the mesh adaptation, we plot in Fig. 8 an adaptive mesh at $t = 3$. It is observed that the mesh represents more or less the same as the solution structure, with more grid points in the regions of the sharp front and the thin filaments. Fig. 9 displays the evolution of the density along the symmetry axis $x = \pi$ at times $t = 0.5, 1, 1.5, 2$ and 2.5. The formation of a front is clearly observed, which is similar to the formation of shock fronts in the solutions of the Burgers equation. Moreover, it is observed in Fig. 9 that the moving mesh solutions are oscillation-free with a 500^2 grid, which is in contrast with the spectral solutions with a 512^2 grid [14].
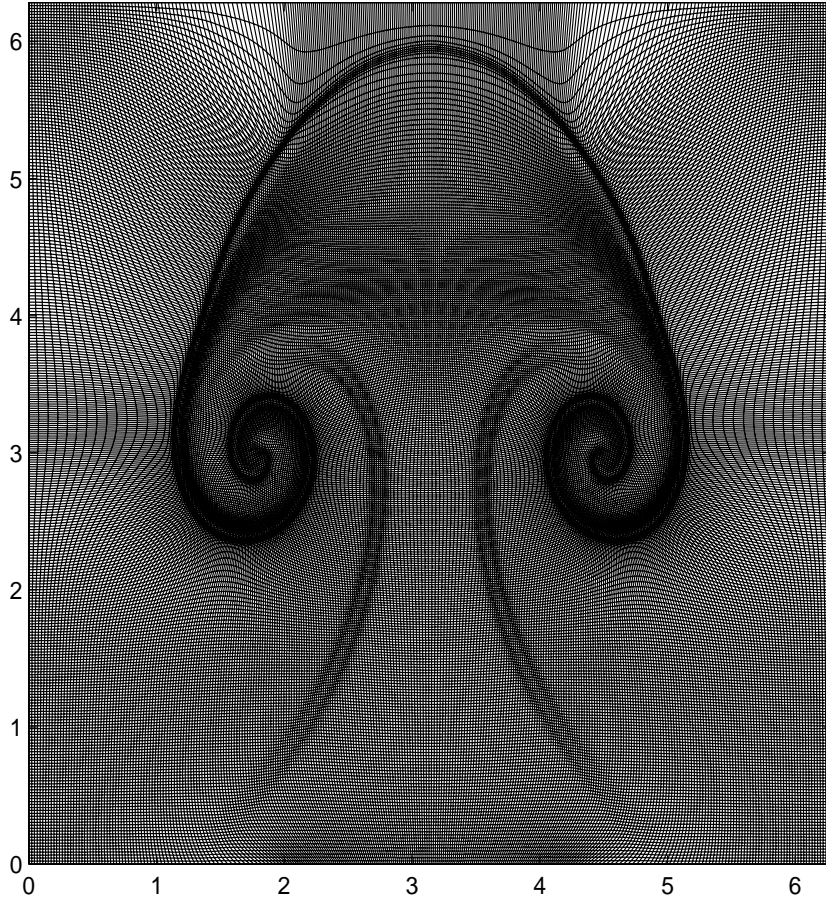
Figure 8: A moving mesh at $t = 3$ with a 300^2 grid.

The largest time calculated by E & Shu [14] is $t = 3.16$, at that time they found a secondary front from the tail vortices. This is also confirmed by our adaptive computations. Fig. 10 shows a cut of vorticity and density profile through the rolls at $t = 3.16$, which is found in good agreement with the fine-mesh solutions given in [14].

Up to the time $t = 3.16$, the results obtained using the Fourier collocation method with Fourier-Padé postprocessing are basically in good agreement with the adaptive mesh computations. However, the spectral simulation can evolve further to the range $3.5 \leq t \leq 4$ while our moving mesh computations are too slow to obtain finer mesh results in this time range. Below we will report some numerical results obtained by using the spectral algorithm. Fig. 11 shows the density and vorticity contours at $t = 3.5$ on a 1024^2 grid. At this time level, the bubble has risen to the upper periodic box so we draw the pictures in the range of $2 \leq y \leq 8$ rather than $0 \leq y \leq 2\pi$. The vortical structures at the bottom of the bubble evolves into two tightly packed rolls. We also plot in Fig. 12 a cut of vorticity and density profile through the rolls at $t = 3.5$, which are found very similar to the coarser mesh results for $t = 3.16$ given in Fig. 10. Due to the high resolution and minimal dissipation of the spectral methods, the tightly packed vortical structures are successfully resolved in a
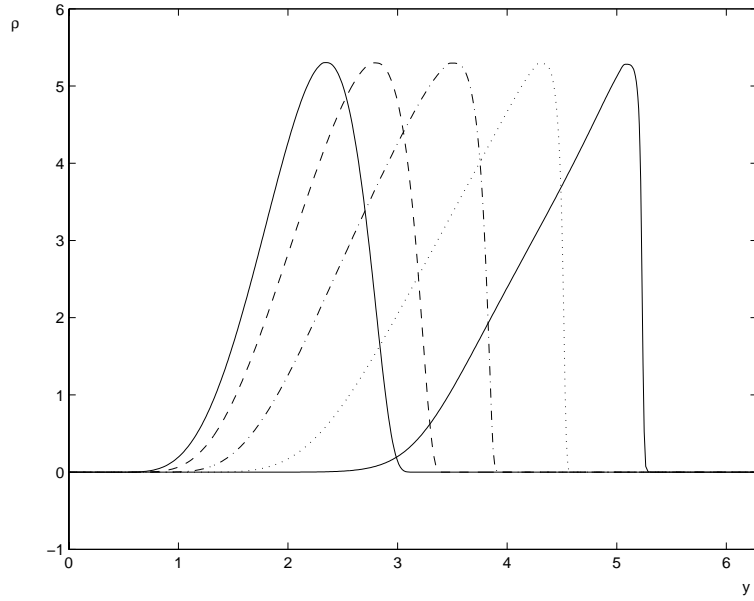
Figure 9: Evolution of density along the symmetry axis $x = \pi$ at $t = 0.5, 1, 1.5, 2, 2.5$.
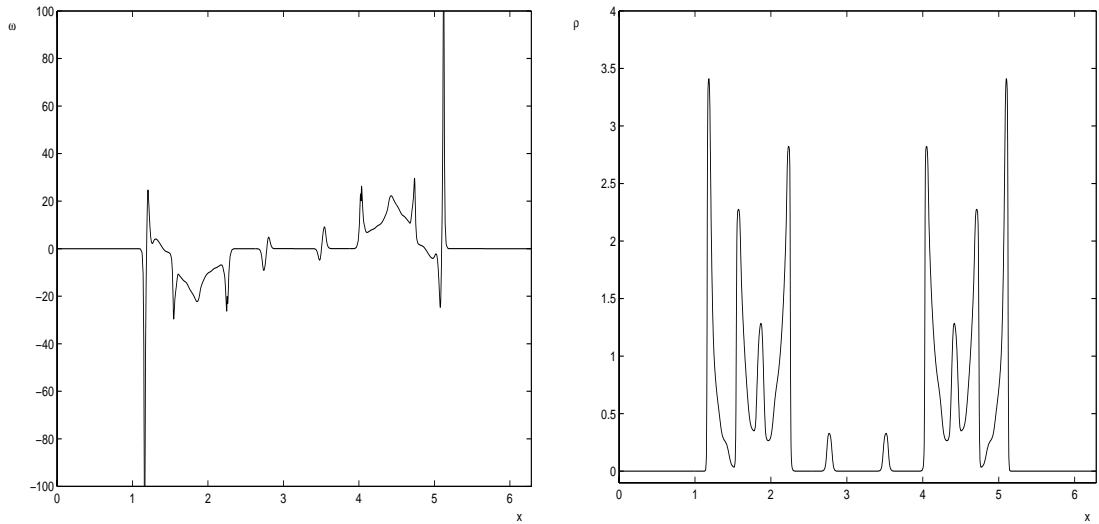

Figure 10: A cut of vorticity profile (left) and the density profile (right) through the roll at $t = 3.16$, on a 500^2 grid.

long time integration even in the presence of the large gradients. The problem at this time level is computed using two grids, namely 768^2 and 1024^2, and the convergence with the mesh refinement seems satisfactory. To see this, we plot in Fig. 13 a cut of density profile through $y = 0.586\pi$ at $t = 3.5$, which is obtained by using the two grids. The agreement of the two curves is very good.

At $t = 4$, the numerical solutions are also obtained by using both the 768^2 and 1024^2 grids. At this time, the flow becomes increasingly complex due to the growth of the small
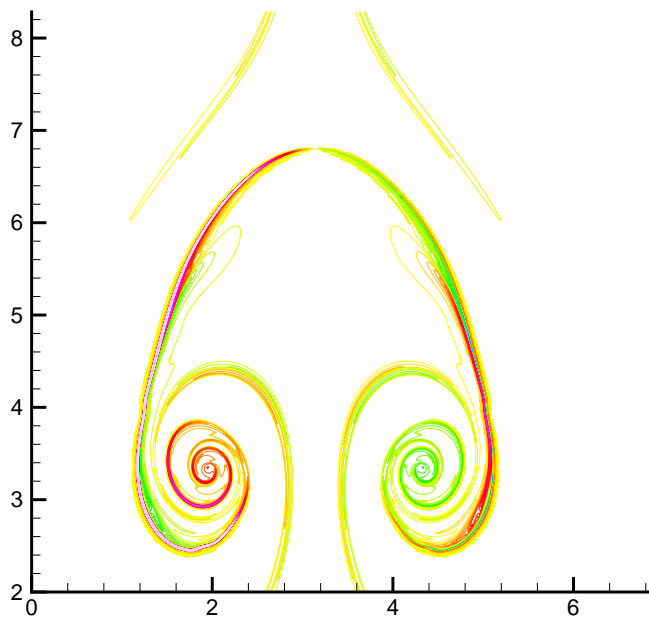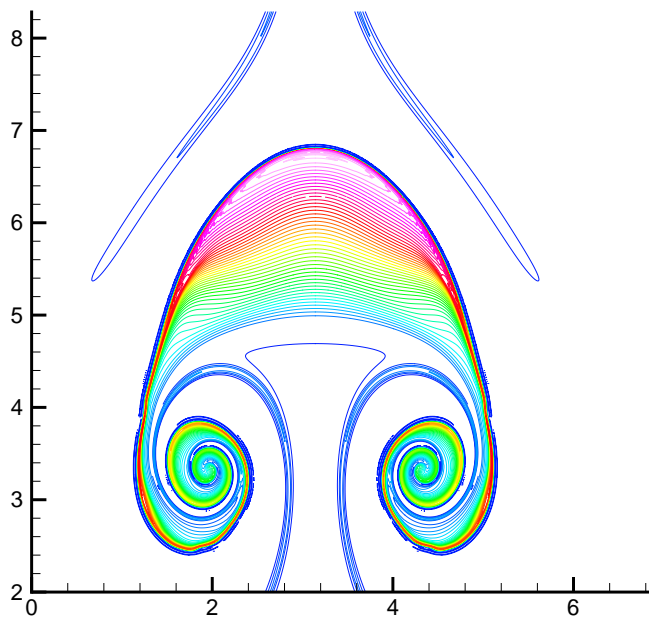
Figure 11: Density (left) and vorticity (right) contour plot at $t = 3.5$. The grid size is 1024^2.

scale structures generated along the side front of the main bubble. By comparing the overall flow structures of the density and vorticity with the two resolutions in Figs. 14
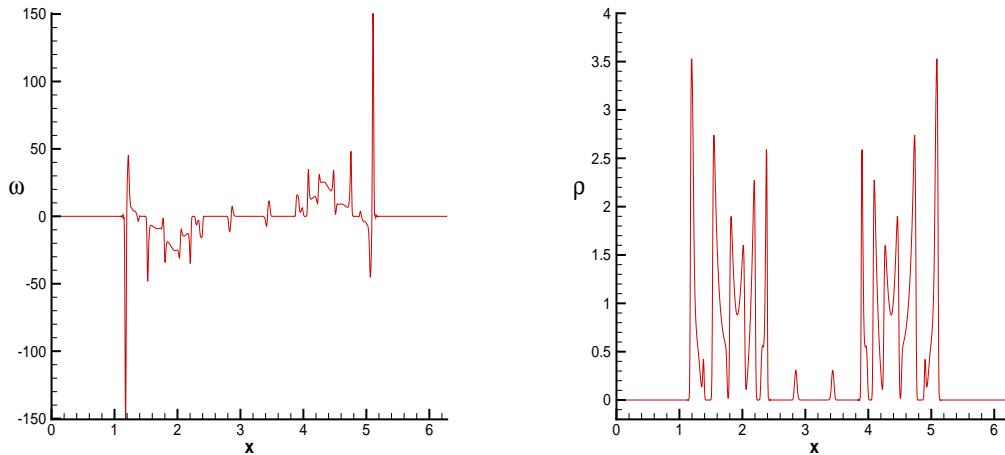
Figure 12: A cut of vorticity profile (left) and the density profile (right) through the roll at $t = 3.5$, on a 1024^2 grid.
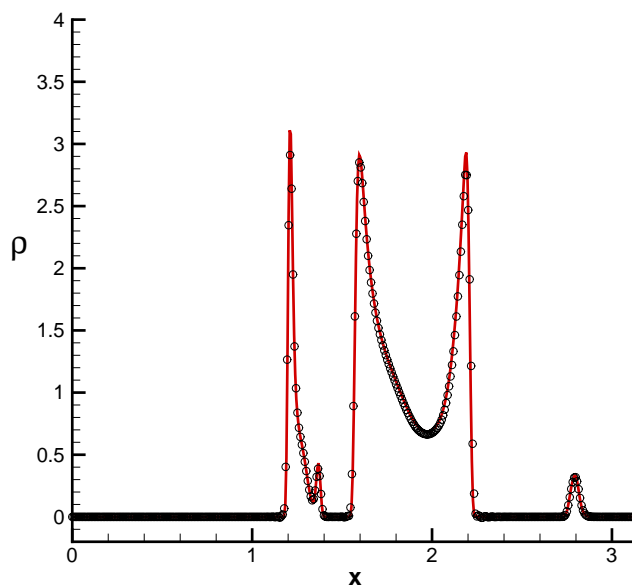

Figure 13: Resolution comparison: a cut of density profile through $y = 0.586\pi$ at $t = 3.5$, using a 1024^2 grid (solid line) and a 768^2 grid (circle).

and 15, we find that the integrity of the complicated large and medium scale structures are captured reasonably well by the spectral simulations. Fig. 16 shows the streamlines and velocity vector over the vorticity contour along the rising bubble front just below the cap. It is observed from these three figures that the shear flow generates the characteristic vortices shedding due to the Kelvin-Helmholtz instability. The velocities across the bubble
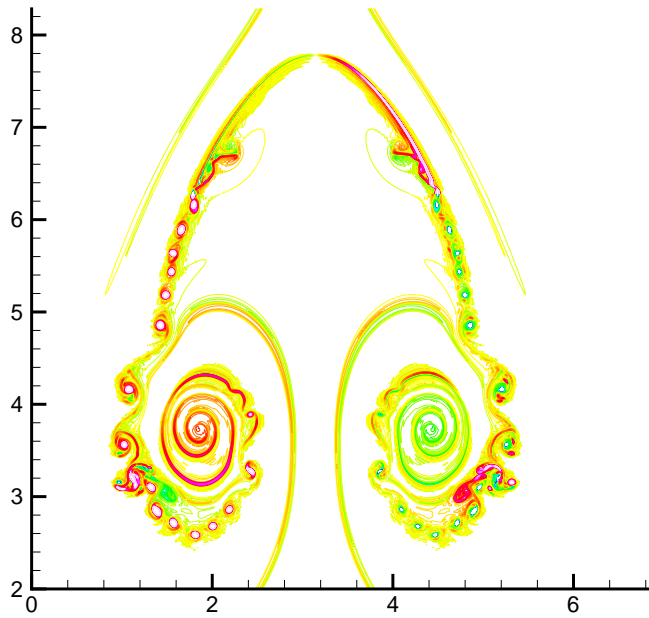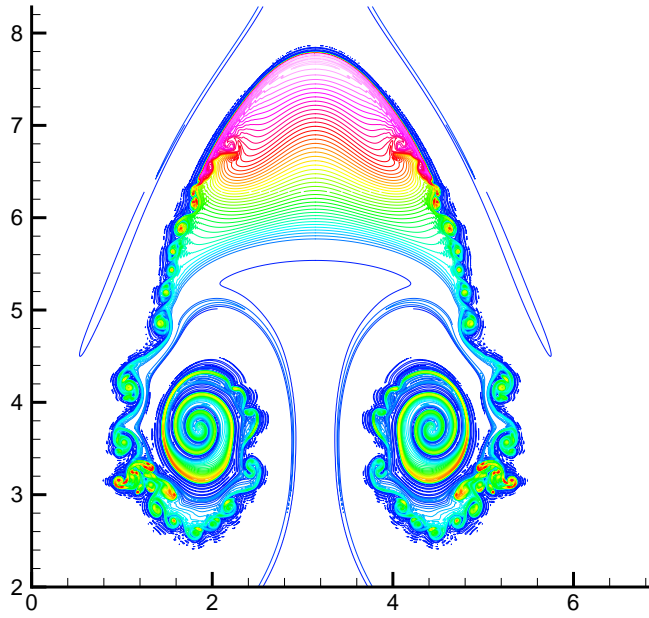
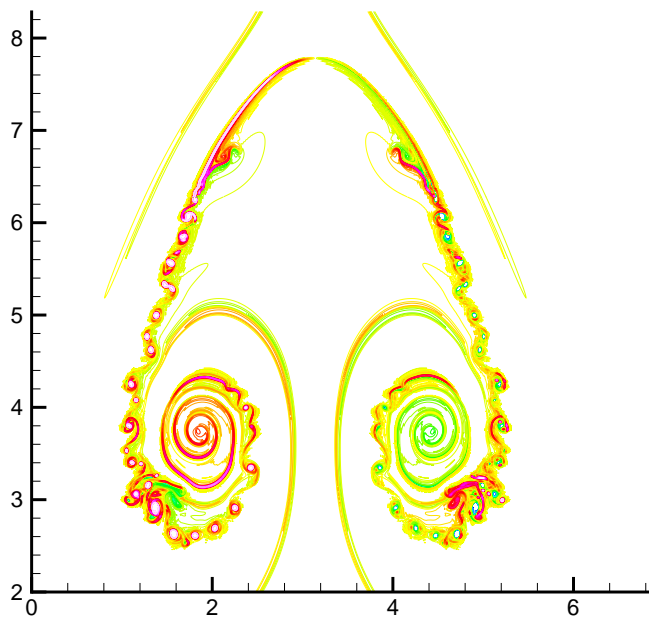Figure 14: Density (left) and vorticity (right) contour plot at $t = 4$. The grid size is 768^2.
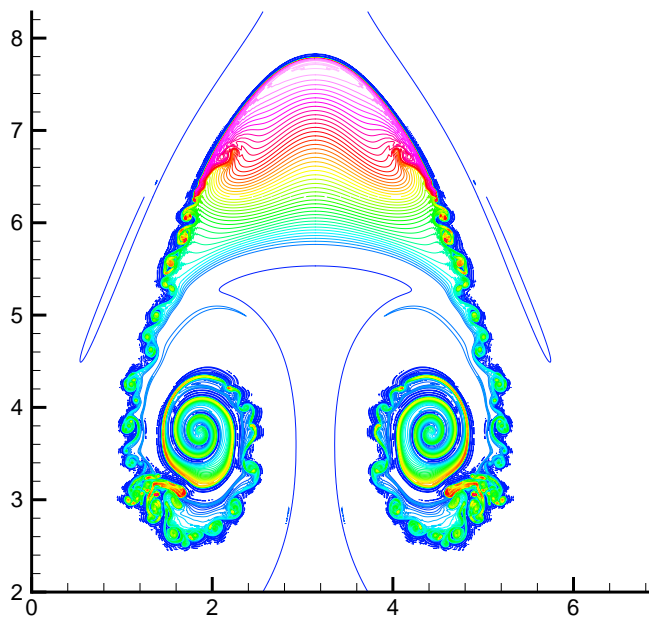
Figure 15: Density (left) and vorticity (right) contour plot at $t = 4$. The grid size is 1024^2.

front have opposite sign. Moreover, the structures along the outer edge of the bubble at $t = 4$ are quite different from the one for $t = 3.5$. One possibility of this phenomena
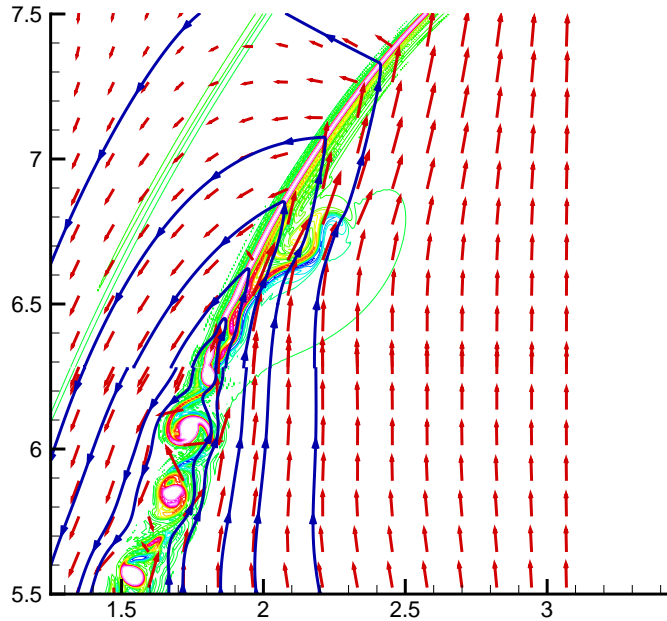
Figure 16: Streamline and velocity vector overlay on top of the vorticity at time $t = 4$, obtained on a 1024^2 grid.

is the interaction between the numerical artifacts (under-resolved front) and the Kelvin-Helmholtz instability due to the velocity shear layer across the front. Conceptual-wise, the front should be stretched infinitely thin with increasing number of roll ups inside the vortical structures if the flow is inviscid and has no external perturbation (noise). However, the thin front is very unstable and subjects to exponential growth of perturbation due to the Kelvin-Helmholtz instability over the shear layer. The numerical noise (Gibbs or otherwise) acts like perturbation in the simulation.

Fig. 17 shows a cut of density profile through $y = 0.586\pi$ at $t = 4$ using the 768^2 and 1024^2 grids. It is observed that in most parts of the domain the agreement is good except near the bubble front, which implies that the mesh resolution is not satisfactory with the 768^2 grid. Unfortunately, our current computer power prevent us from obtaining finer mesh results. It will be interesting to further improve our moving mesh methods and the spectral methods so that finer mesh results can be obtained and being used for comparisons.

It is our conjecture that no matter how well the flow is resolved numerically initially, the flow will eventually exhibit similar features as shown in Fig. 15 unless sufficient numerical viscosity existed to smear out the shear layer and the front. This is also in agreement with the recent computations of Yamada et al. [32] where extremely fine meshes are used in their AMR algorithms. In [23], Matsumoto et al. solves the 2D Boussinesq problem with
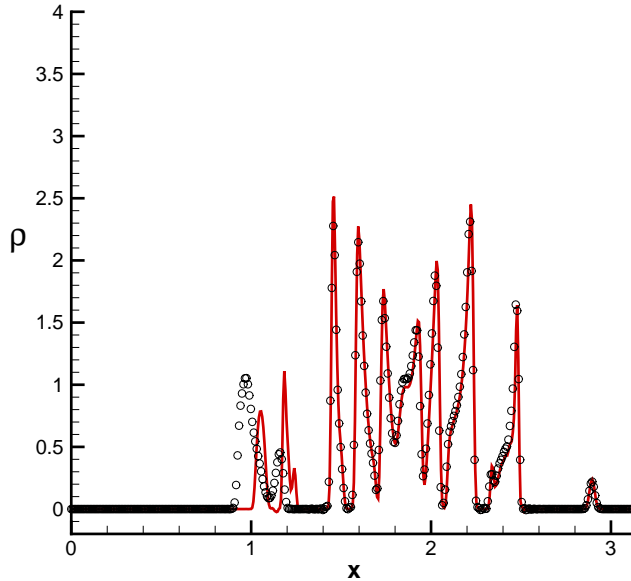
24

Figure 17: Resolution comparison: a cut of density profile through $y = 0.586\pi$ at $t = 4$, using a 768^2 (circle) and a 1024^2 (solid line) grid.

an adaptive mesh refinement (AMR) technique based on a second-order MUSCLE scheme. The smallest adapted-mesh size in the adaptive computations is about $2\pi/2^{15} \approx 2 * 10^{-4}$. Their results, with a different (smooth) initial data, also suggest that a finite-time blow-up may occur around $t > 4$ and the density gradient and the vorticity diverge at rates

$$(5.1) \qquad\qquad |\rho|_\infty \sim (t_0 - t)^{-2}, \qquad |\omega| \sim (t_0 - t)^{-1}$$

respectively, where $t_0 \approx 6$.

6   Concluding Remarks

In this work, we have employed two high-resolution numerical methods, namely the moving mesh method and the Fourier spectral method, to numerically solve the two-dimensional equations for Boussinesq convection. The initial conditions for our computations were taken from E & Shu [14], which consist of a smooth bubble of density. This problem has generated many theoretical interests in the past. The rapid formation of small scales and the possible finite-time blow-up make this problem very challenging for numerical simulations. The aim of this project is to obtain reliable numerical solutions for larger time, and to see whether finite-time blow-up occurs for initially smooth flows. This study has confirmed the earlier findings of E & Shu [14], and also extended their numerical computations beyond $t = 3.16$. At $t = 4$, our numerical result with an 1024^2 grid suggests a finite-time blow-up for the

Boussinesq convection problem. This is in good agreement with the recent computations of Yamada et al. [32] and of Matsumoto et al. [23] who have used extremely fine meshes in the computations.

It will be interesting to further improve our numerical methods so that more reliable numerical solutions can be obtained on fine meshes. A website related to the numerical results of this work and some other incompressible flow simulations can be found in the following website:

http://www.math.hkbu.edu.hk/~ttang/MMmovie/NS

References

[1] B.N. Azarenok, S.A. Ivanenko and T. Tang, *Adaptive mesh redistribution method based on Godunov's scheme*, Communication on Mathematical Sciences, 1 (2003), pp. 152-179.

[2] R.H. Bartels, G.W. Stewart, *Algorithm 432, solution of the matrix equation $Ax + xB = C$*, Comm. ACM, 15 (1972), pp. 820-826.

[3] J. T. Beale, T. Kato and A. Majda, *Remarks on the breakdown of smooth solutions for the 3-D Euler equations*, Comm. Math. Phys., 94 (1984), p. 61.

[4] M. J. Berger and J. Oliger, *Adaptive mesh refinement for hyperbolic partial differential equations*, J. Comput. Phys., 53 (1984), pp. 484-512.

[5] M. E. Brachet, D. I. Meiron, S. A. Orszag, B. G. Nickel, R. H. Morf and U. Frisch *Small-scale structure of the Taylor-Green vortex*, J. Fluid Mech., **130**(1983), pp. 411-452.

[6] W. S. Don, D. Gottlieb, C. W. Shu, O. Schilling and L. Jameson, *Convergence study of inviscid Taylor-Green vortex flow*, J. Sci. Comput., Accepted, 2003.

[7] J.U. Brackbill and J.S. Slatzman, *Adaptive zoning for singular problems in two dimensions.* J. Comput. Phys., 46 (1982), pp. 342-368.

[8] W.M. Cao, W.Z. Huang and R.D. Russell, *An r-adaptive finite element method based upon moving mesh PDEs*, J. Comput. Phys. 149 (1999), pp. 221-244.

[9] H. D. Ceniceros and T. Y. Hou, *An efficient dynamically adaptive mesh for potentially singular solutions.* J. Comput. Phys., 172 (2001), pp. 609-639.

[10] B. Costa and W. S. Don, *On the computation of high order pseudospectral derivatives*, Appl. Numer. Math., 33 (2000), pp. 151-159.

[11] W. S. Don, *Numerical study of pseudospectral methods in shock wave applications*, J. Comput. Phys., 110 (1994), pp. 103-111.

[12] T.A. Driscoll and B. Fornberg, *A Padé-based algorithm for overcoming the Gibbs' phenomenon*, Numerical Algorithms, 26 (2001), pp. 77-92.

[13] A. Dold and B. Eckmann, *Pade Approximation and its Application*, Springer-Verlag, Berlin Heidelberg, New York, 1979.

[14] Weinan E and C.W. Shu, *Small-scale structures in Boussinesq convection*, Phys. Fluids, 6 (1994), p. 49.

[15] L. Emmel, S.M. Kaber and Y. Maday *Padé-Jacobi filtering for spectral approximations of discontinuous solutions.* To appear in Numerical Algorithms, 2003.

[16] J.F. Geer *Rational trigonometric approximations using Fourier series partial sums*, J. Sci. Comput., **10** (1995), pp. 325-356.

[17] D. Gottlieb, M. Y. Hussaini and S. A. Orszag, *Introduction: Theory and Applications of Spectral Methods*, in Spectral Methods for Partial Differential Equations, R. Voigt, D. Gottlieb and M.Y. Hussaini, ed., SIAM, Philadelphia, 1984. pp. 1-54.

[18] D. Gottlieb, S. A. Orszag, *Numerical Analysis of Spectral Methods : Theory and Application*, CMBS-NSF Regional Conference Series in Applied Mathematics 26, SIAM, Philadelphia, 1977.

[19] R. Grauer, C. Marliani and K. Germaschewski. *Adaptive mesh refinement for singular solutions of the incompressible Euler equations.* Phys. Rev. Lett., 80 (1998), pp. 4177-4180.

[20] R. Grauer and T. C. Sideris. *Numerical computation of 3D incompressible ideal fluids with swirl,* Phys. Rev. Lett., 67 (1991), pp. 3511-3514.

[21] R. Grauer and T. C. Sideris. *Finite time singularities in ideal fluids with swirl,* Physica D, 88 (1995), pp. 116-132.

[22] R. Li, T. Tang and P. Zhang, *Moving mesh methods in multiple dimensions based on harmonic maps.* Journal of Computational Physics, 170 (2001), pp. 562-588.

[23] T. Matsumoto, H. Miyashita, Y. Yamada and S. Toh, *A numerical search for a singularity of 2D inviscid Boussinesq approximation equation,* Workshop on Progress in Statistical Hydrodynamics, Center for Nonlinear Studies, Los Alamos National Lab., 2002.

[24] M. S. Min, S. M. Kaber and W. S. Don, *Fourier-Padé approximations and filtering for the spectral simulations of incompressible Boussinesq convection problem,* J. Sci. Comput., To appear.

[25] A. Pumir and E. D. Siggia. *Development of singular solutions to the axisymmetric Euler equations,* Phys. Fluids, A4 (1992), pp. 1472-1491.

[26] A. Pumir and E. D. Siggia. *Finite-time singularities in the axisymmetric three-dimensional Euler equations,* Phys. Rev. Lett., 68 (1992), pp. 1511-1514.

[27] E.B. Saff and R.S. Vargra, *Pade and Rational Approximation: Theory and Application,* Academic Press, New York, 1977.

[28] C.-W. Shu and S. Osher, *Efficient implement of essentially non-oscillatory shock-wave schemes, II,* J. Comput. Phys., 83 (1989), pp. 32-78.

[29] H.Z. Tang and T. Tang, *Moving mesh methods for one– and two–dimensional hyperbolic conservation laws,* SIAM J. Numer. Anal., 41 (2003), pp. 487-515.

[30] H. Vandeven, *Family of spectral filters for discontinuous problems,* J. Sci. Compt., 6 (1991), p. 159.

[31] A. Winslow, *Numerical solution of the quasi-linear Poisson equation on a nonuniform triangle mesh,* J. Comput. Phys., 1 (1967), pp. 149-172.

[32] Y. Yamada, H. Miyashita, S. Toh and T. Matsumoto, *Simulation of finite time divergence in 2D Boussinesq equation by adaptive mesh code,* Proceedings of Annual Meeting of Japan Society of Fluid Mechanics, 2001, (in Japanese).
http://www.amesh.org/pub/0003/index.html.

[33] Z.-R. Zhang, *Moving-Mesh Methods for Convection-Dominated Equations and Nonlinear Conservation Laws,* PhD Thesis, Dept of Mathematics, Hong Kong Baptist University, 2003.

[34] Z.R. Zhang and T. Tang, *An adaptive mesh redistribution algorithm for convection-dominated problems,* Communication on Pure and Applied Analysis, 1 (2002), pp. 57-73.